Optical differentiation wavefront sensing with binary pixelated transmission filters

J. Qiao,[1,2,*] Z. Mulhollan,[1] and C. Dorrer[2]

[1]*Chester F. Carlson Center for Imaging Science, Rochester Institute of Technology, 54 Lomb Memorial Drive, Rochester, NY 14623, USA*

[2]*Aktiwave LLC, 241 Ashley Drive, Rochester, NY 14620, USA*

[*]*qiao@cis.rit.edu*

Abstract: Sensors measuring the spatial phase of optical waves are widely used in optics. The optical differentiation wavefront sensor (ODWS) reconstructs the wavefront of an optical wave from wavefront slope measurements obtained by inducing linear field-transmission gradients in the far-field. Its dynamic range and sensitivity can be adjusted simply by changing the gradient slope. We numerically and experimentally demonstrate the possibility of implementing the spatially varying transmission gradient using distributions of small pixels that are either transparent or opaque. Binary pixelated filters are achromatic and can be fabricated with high accuracy at relatively low cost using commercial lithography techniques. We study the impact of the noise resulting from pixelation and binarization of the far-field filter for various test wavefronts and sensor parameters. The induced wavefront error is approximately inversely proportional to the pixel size. For an ODWS with dynamic range of 100 rad/mm over a 1-cm pupil, the error is smaller than λ/15 for a wide range of test wavefronts when using 2.5-μm pixels. We experimentally demonstrate the accuracy and consistency of a first-generation ODWS based on binary pixelated filters.

OCIS codes: (120.5050) Phase measurement; (070.0070) Fourier optics and signal processing.

References and links

1. D. Malacara, *Optical Shop Testing*, 3rd ed. (John Wiley and Sons, 2007).
2. F. Z. Fang, X. D. Zhang, A. Weckenmann, G. Z. Zhang, and C. Evans, "Manufacturing and measurement of freeform optics," CIRP Annals - Manufacturing Technol. **62**, 823–846 (2013).
3. J. Néauport, X. Ribeyre, J. Daurios, D. Valla, M. Lavergne, V. Beau, and L. Videau, "Design and optical characterization of a large continuous phase plate for Laser Integration Line and Laser Megajoule facilities," Appl. Opt. **42**(13), 2377–2382 (2003).
4. H. I. Campbell and A. H. Greenaway, "Wavefront sensing: from historical roots to the state-of-the-art," EAS Publications Series **22**, 165–185 (2006).
5. J.-P. Zou and B. Wattellier, "Adaptive optics for high-peak-power lasers – an optical adaptive closed-loop used for high-energy short-pulse laser facilities: laser wave-front correction and focal-spot shaping," in *Topics in Adaptive Optics*, Bob Tyson ed. (Intech, 2012).
6. J. Porter, A. Guirao, I. G. Cox, and D. R. Williams, "Monochromatic aberrations of the human eye in a large population," J. Opt. Soc. Am. A **18**(8), 1793–1803 (2001).
7. J. W. Cha, J. Ballesta, and P. T. So, "Shack-Hartmann wavefront-sensor-based adaptive optics system for multiphoton microscopy," J. Biomed. Opt. **15**(4), 046022 (2010).
8. B. C. Platt and R. Shack, "History and principles of Shack-Hartmann wavefront sensing," J. Refract. Surg. **17**(5), S573–S577 (2001).
9. J.-C. Chanteloup, "Multiple-wave lateral shearing interferometry for wave-front sensing," Appl. Opt. **44**(9), 1559–1571 (2005).
10. F. Roddier, "Curvature sensing and compensation: a new concept in adaptive optics," Appl. Opt. **27**(7), 1223–1225 (1988).
11. W. Zou, K. P. Thompson, and J. P. Rolland, "Differential Shack-Hartmann curvature sensor: local principal curvature measurements," J. Opt. Soc. Am. A **25**(9), 2331–2337 (2008).

#260640 Received 7 Mar 2016; revised 11 Apr 2016; accepted 11 Apr 2016; published 19 Apr 2016

12. R. A. Sprague and B. J. Thompson, "Quantitative visualization of large variation phase objects," Appl. Opt. **11**(7), 1469–1479 (1972).
13. J. C. Bortz, "Wave-front sensing by optical phase differentiation," J. Opt. Soc. Am. A **1**(1), 35–39 (1984).
14. J. E. Oti, V. F. Canales, and M. P. Cagigal, "Improvements on the optical differentiation wavefront sensor," Mon. Not. R. Astron. Soc. **360**(4), 1448–1454 (2005).
15. M. P. Cagigal and P. J. Valle, "x-y curvature wavefront sensor," Opt. Lett. **40**(8), 1655–1658 (2015).
16. T. Szoplik, V. Climent, E. Tajahuerce, J. Lancis, and M. Fernández-Alonso, "Phase-change visualization in two-dimensional phase objects with a semiderivative real filter," Appl. Opt. **37**(23), 5472–5478 (1998).
17. A. Sagan, T. J. Antosiewicz, and T. Szoplik, "Three filters for visualization of phase objects with large variations of phase gradients," Appl. Opt. **48**(6), 1143–1152 (2009).
18. W. Zou and J. P. Rolland, "Quantifications of error propagation in slope-based wavefront estimations," J. Opt. Soc. Am. A **23**(10), 2629–2638 (2006).
19. F. Henault, "Wavefront sensor based on varying transmission filters: theory and expected performance," J. Mod. Opt. **52**(14), 1917–1931 (2005).
20. J. Oti, V. Canales, and M. Cagigal, "Analysis of the signal-to-noise ratio in the optical differentiation wavefront sensor," Opt. Express **11**(21), 2783–2790 (2003).
21. O. von der Lühe, "Wavefront error measurement technique using extended, incoherent light sources," Opt. Eng. **27**, 1078–1087 (1988).
22. C. Dorrer and J. D. Zuegel, "Design and analysis of binary beam shapers using error diffusion," J. Opt. Soc. Am. B **24**(6), 1268–1275 (2007).
23. D. Schmidt and O. von der Lühe II, "Optical wavefront differentiation: wavefront sensing for solar adaptive optics based on a LCD," Proc. SPIE **6584**, 658408 (2007).
24. H. Furuhashi, J. Valle Mayorga, Y. Uchida, and A. Kono, "Phase measurement of optical wavefront by an SLM differentiation filter," in *XIX IMEKO World Congress Fundamental and Applied Metrology* (2009), pp. 1–5.
25. E. Gendron, M. Brangier, G. Chenegros, F. Vidal, Z. Hubert, G. Rousset, and F. Pouplard, "A new sensor for laser tomography on ELTs," in *1st AO4ELT Conference* (2010), paper 05003.
26. H. Furuhashi, K. Matsuda, and C. P. Grover, "Visualization of phase objects by use of a differentiation filter," Appl. Opt. **42**(2), 218–226 (2003).
27. C. Dorrer, "Analysis of the chromaticity of near-field binary beam shapers," Appl. Opt. **52**(14), 3368–3380 (2013).
28. P. Martinez, C. Dorrer, M. Kasper, A. Boccaletti, and K. Dohlen, "Design, analysis, and testing of a microdot apodizer for the apodized pupil Lyot coronagraph," Astron. Astrophys. **495**(1), 363–370 (2009).
29. R. Ulichney, *Digital Halftoning* (MIT Press, 1987).
30. W. H. Southwell, "Wave-front estimation from wave-front slope measurements," J. Opt. Soc. Am. **70**(8), 998–1006 (1980).
31. C. Genet and T. W. Ebbesen, "Light in tiny holes," Nature **445**(7123), 39–46 (2007).
32. C.-P. Huang and Y.-Y. Zhu, "Plasmonics: manipulating light at the subwavelength scale," in *Active and Passive Electronic Components 2007* (2007), paper 30946.
33. P. Murphy, J. Fleig, G. Forbes, D. Miladinovic, G. DeVries, and S. O'Donohue, "Subaperture stitching interferometry for testing mild aspheres," Proc. SPIE **6293**, 62930J (2006).

1. Introduction

Measuring the wavefront of optical waves is fundamental to many aspects of optics and expands to various areas of physics. Assessing the wavefront induced by an optical component is required for many applications and is often required during the manufacturing process. The need for accurate wavefront metrology closely follows the quickly evolving ability to manufacture complex optical components introducing large phase gradients, such as freeform optics for imaging or phase plates for spatial coherence control [1–3]. Wavefront measurements are important in astronomy to correct for turbulence by adaptive optics and operate a telescope close to its theoretical diffraction limit [4]. The same consideration applies in laser engineering, where wavefront distortions of the laser beam must be understood and corrected to maximize the on-target intensity [5]. The role of wavefront metrology is increasing in a large range of biomedical applications [6,7]. There is a multitude of techniques to measure the spatial phase of an optical wave. Test + reference interferometry (e.g. Fizeau interferometer) is well suited to characterize the wavefront distortion induced by a component under test relative to a reference wave [1]. Shack-Hartmann wavefront sensors are commonly used for wavefront measurements when no reference wave is available, for example in laser systems [8]. There are also self-referencing techniques that rely on self-interference of the unknown test wave [1,9] and on determinations of the curvature of the wavefront under test [10,11].

#260640 Received 7 Mar 2016; revised 11 Apr 2016; accepted 11 Apr 2016; published 19 Apr 2016

Visualization of phase objects by converting phase modulation into an observable amplitude modulation was demonstrated by Sprague and Thompson [12]. The more general implementation of an optical differentiation wavefront sensor (ODWS) based on several wavefront gradients obtained by amplitude modulation in a coherent filtering setup was pioneered by Bortz [13]. It requires a spatially varying transmission filter in the far field of the source under test. The implementation described here is based on a single linear field-transmission function used in two perpendicular orientations, but other transmission profiles and experimental arrangements have been investigated [14–17]. With a linear field-transmission modulation, the fluence measured in the image plane of the pupil is related to the wavefront slope in the direction of the transmission gradient. The measurement of two wavefront slopes in non-parallel directions is necessary and sufficient to reconstruct the wavefront in the pupil plane, with orthogonal measurements being a natural, but not necessary, choice. The wavefront can be reconstructed with algorithms identical to those used for Shack-Hartmann wavefront sensors because the latter intrinsically provide wavefront-slope data in two orthogonal directions [18]. The principle of the ODWS is simple and its potential advantages have been studied [19–21]. In particular, simulations and analysis have shown that an ideal ODWS can compare favorably with Shack-Hartmann sensors in terms of signal-to-noise ratio and dynamic range. Compared to most interferometric techniques, the ODWS does not have a strong coherence requirement, e.g., can operate with non-monochromatic sources. Despite these advantages, the ODWS is not widely used, which can be attributed in part to the practical difficulty of manufacturing components with well-controlled transmission profiles.

In this article, we demonstrate that a high-performance ODWS can be implemented with binary pixelated amplitude filters. These filters synthesize the continuously spatially varying transmission function with spatially dithered distributions of opaque or transparent pixels [22]. They can be manufactured with high precision using conventional commercial lithography techniques, but the binarization and pixelation introduce noise that impact the measurement accuracy. We show that an ODWS implemented with a binary pixelated filter (thereafter referred to as BPF-ODWS) is a viable technical solution to characterize non-trivial wavefronts, in particular those encountered for optical systems alignment, laser characterization, and during the manufacturing and testing of freeform optics. Some general scaling rules for the wavefront-sensor parameters are derived. The general principle of the ODWS and technological solutions for its implementation are decribed in Section 2. Section 3 introduces the BPF-ODWS and considerations about the pixel size. Sections 4 and 5 present the detailed study of a BPF-ODWS and comparative performance with an ideal ODWS. Finally, Section 6 presents the experimental demonstration of a BPF-ODWS.

2. General considerations on the ODWS

2.1. Principle

The ODWS reconstructs the wavefront of an optical wave from two wavefront-gradient measurements that are assumed in this article to be performed in orthogonal directions. The wavefront gradient in the x direction is obtained by applying a filter with a field transmission linear in that direction in the far field of the source, for example in a coherent processing setup [13], as shown in Fig. 1. The field at the input pupil is Fourier transformed to the far field by the combination of propagation by a distance f, propagation in a thin lens of focal length f, and additional propagation by a distance f. The spatially varying transmission filter is set in the Fourier plane. After spatial modulation, the field is inverse Fourier transformed to the detection plane. Without filter, the fluence $F_0(x,y)$ measured in that plane is identical to the input fluence, after taking into account an obvious spatial inversion. To provide phase sensitivity, a filter defined by

#260640 Received 7 Mar 2016; revised 11 Apr 2016; accepted 11 Apr 2016; published 19 Apr 2016

$$t(u,v) = \frac{1}{2} + \frac{u}{W}, \tag{1}$$

where W is the full width of the filter, is located in the far field. Provided that the far field of the source under test is fully encompassed in the linear region of the filter defined by $-W/2<u<W/2$, the detected fluence $F_x(x,y)$ allows for the determination of the wavefront slope using

$$\frac{\partial \phi}{\partial x} = \frac{\pi W}{\lambda f}\left[2\sqrt{\frac{F_x}{F_0}} - 1\right]. \tag{2}$$

An orthogonal wavefront slope is determined with the same setup after rotating the filter by 90 degrees, yielding

$$\frac{\partial \phi}{\partial y} = \frac{\pi W}{\lambda f}\left[2\sqrt{\frac{F_y}{F_0}} - 1\right]. \tag{3}$$

The input wavefront can be reconstructed from the two wavefront slopes given by Eqs. (2) and (3), in a manner analogous to wavefront reconstruction with Shack-Hartmann sensors and spatial shearing interferometry [18]. When the 4f line is built with achromatic components, the imaging condition between input and output is wavelength-independent, allowing for operation with monochromatic and narrowband sources at different wavelengths. Operation with sources having a broad optical spectrum is possible [20], but the averaging process and resulting accuracy have not been thoroughly investigated.

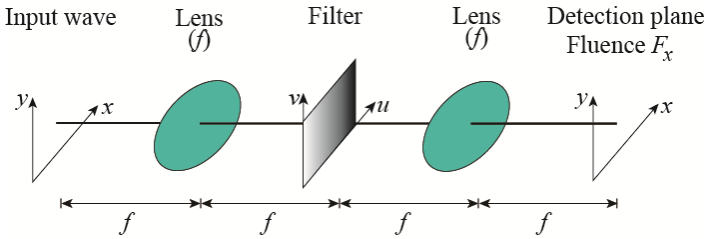

Fig. 1. Principle of the optical differentiation wavefront sensor. A filter with linear field transmission gradient is located at the Fourier plane of a 4f line.

2.2. Dynamic range and sensitivity

The derivation in the previous subsection requires that the far-field of the wave under test is fully encompassed in the filter region with linear field transmission extending from -W/2 to W/2. The filter width defines the wavefront-measurement dynamic range as $DR = 2\pi W/(\lambda f)$. For a given λ, DR can be increased by increasing the filter width W and decreasing the focal length f. Increasing the filter width is in general straightforward and is only limited in practice by the technology used to fabricate the filter. Decreasing the focal length is in general possible for an ODWS implemented with an ideal continuous filter, but it will be shown in Section 5 that this decreases the reconstruction accuracy.

Equations (2) and (3) show that the ODWS sensitivity is inversely proportional to the filter width W. For a given input wavefront, the difference between detected modulated fluences F_x and F_y and the fluence in the absence of filter F_0 decreases when W is increased. In practical situations where detection noise is considered, large values of the filter width corrupt the measurement of relatively small phase variations. Therefore there is an intrinsic tradeoff between dynamic range and sensitivity, as is common in metrology. For the ODWS,

#260640 Received 7 Mar 2016; revised 11 Apr 2016; accepted 11 Apr 2016; published 19 Apr 2016

dynamic range and sensitivity can be tuned by adequate choice of the filter width, leading to a practical advantage compared to Shack-Hartmann wavefront sensors [20].

2.3. Technological solutions for the ODWS spatially varying transmission filter

Technologies that can implement the linear field-transmission filter required for an ODWS are now briefly reviewed and discussed. ODWS's based on programmable liquid-crystal spatial light modulator (LC-SLM) have been demonstrated [23,24]. These devices have the advantage of being fully reconfigurable, therefore allowing for filters with different slope magnitude and direction to be generated. In principle, the transmission-vs-voltage transfer function can be calibrated for precise amplitude modulation at the Fourier plane, but the resulting transmission is wavelength-dependent. This implies that different calibrations are required for use at different wavelengths and simultaneous operation at multiple wavelengths, e.g. when characterizing a polychromatic source, might have reduced accuracy. An LC-SLM is fundamentally polarization-dependent and its application is therefore limited to the characterization of well-polarized sources. Pixelated SLM's, even with high fill factors, lead to potentially detrimental diffraction orders. Filters based on a metal layer with spatially varying thickness can in principle be used for an ODWS. Commercially available filters can provide an optical density (OD) that is a linear function of a spatial coordinate, e.g., varying linearly between OD~0 and OD~2 over 3 inches. The optical density is proportional to the thickness of the metal layer for a metal of linear susceptibility. Components with a linear field-transmission function correspond to a complex variation of the deposition time. They can in principle be manufactured but do not seem to be commercially available. A custom component inducing spatially varying optical activity has been successfully used in the context of wavefront sensing for astronomy [25]. Holographic film has been used to visualize phase variations [26]. While some of these approaches have led to successful quantitative phase reconstruction with an ODWS, it is of interest to study and implement novel approaches.

Distributions of small pixels that are either transparent or opaque can synthesize continuous spatially varying transmission functions, as explained in the next section. They can be accurately manufactured as metal-on-glass components by widely available commercial lithography techniques applicable to a variety of metals and substrates at large aperture. Their spatially varying transmission is achromatic [27]. They have been successfully used for laser beam shaping [22] and coronagraphy for astronomical telescopes [28], but they have not been theoretically investigated or experimentally used for wavefront sensing with an ODWS.

3. ODWS with binary pixelated filter

3.1. Principle of binary pixelated filter

Binary pixelated filters consist of distributions of transparent or opaque pixels. The pixel distribution corresponding to a particular design (e.g., a linear field-transmission ramp) is calculated using a spatial dithering algorithm [29]. Binarization and pixelation imply that the design transmission cannot be exactly obtained, but efficient spatial dithering algorithms such as error diffusion lead to filters that provide the correct transmission when locally averaged. Preferred spatial dithering filters produce noise that is concentrated at high frequencies and that has no density at zero spatial frequency, i.e., on axis. When a binary pixelated filter is used for spatial beam shaping in the near field, the noise can be removed by a pinhole in the far field of the shaped beam [22]. When a binary pixelated filter is used in the far field of the pupil in an ODWS, the filter noise is in the detection plane. Corruption of the measured fluences F_x and F_y by the filter noise decreases the accuracy of the ODWS compared to an ideal ODWS with a continuous filter.

#260640 Received 7 Mar 2016; revised 11 Apr 2016; accepted 11 Apr 2016; published 19 Apr 2016

3.2. Pixel size considerations

For all the simulations presented in this article excepted in Section 5, a round 1-cm-diameter input pupil, a 4*f* line with f = 1 m, and an optical wave at λ = 633 nm (HeNe laser) are considered. The sampling size du in the Fourier plane is set to the pixel size w of the filter, and the number of points N is adjusted to keep the total width of the Fourier plane constant, i.e., 2048 samples are used for 10-μm pixels, 4096 samples for 5-μm pixels, and 8192 pixels for 2.5-μm pixels. This keeps the sampling in the measurement plane dx constant because $dx = f\lambda/(Ndu)$. A linear-transmission filter with W = 1 cm is used. This set of parameters yields DR~100 rad/mm. Binary pixelated filters are designed using a four-weight error-diffusion algorithm [22,29] applied to the field transmission t defined by:

$$t(u,v) = \frac{1}{2} + \frac{u}{W} \text{ for } -W/2 < u < W/2 \tag{4}$$

$$t(u,v) = 0 \text{ for } u < -W/2 \tag{5}$$

$$t(u,v) = 1 \text{ for } u > W/2 \tag{6}$$

Figure 2 shows the fluence F_y in the detection plane on a logarithmic scale for a continuous filter and for binary pixelated filters with pixel size of 10 μm, 5 μm, and 2.5 μm. The noise due to the binary pixels is clearly seen and is being pushed at higher frequencies away from the image of the 1-cm pupil when the pixel size decreases.

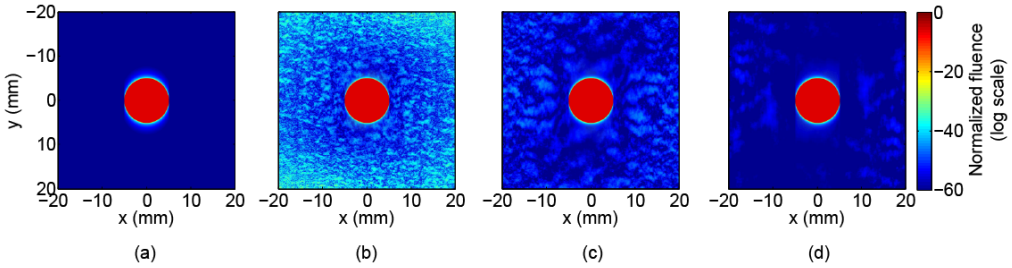

Fig. 2. Fluence in the detection plane plotted on a logarithmic scale for (a) a continuous filter, (b), (c), and (d) binary pixelated filters with 10-μm, 5-μm, and 2.5-μm pixels, respectively. The input pupil (1-cm diameter) is reimaged to the detection plane and appears as a disk with 25% of the fluence of the input beam.

The binary pixelated filter synthesizes a continuous filter when there is a large number of pixels across any feature in the far field. The smallest far-field feature for an input pupil of size S is of the order of $\lambda f/S$, hence the condition for pixel size of $w << \lambda f/S$ for a BPF- ODWS is required for performance similar to that of an ideal ODWS. It should be noted that this only guarantees similar relative performance: wavefronts with slopes exceeding the dynamic range will have similar low reconstruction accuracy with a continuous and pixelated filter. Figure 3 shows the lineout of the fluence at the Fourier plane and the transmission of various filters. The diameter of the far-field main lobe, calculated as the width between the two zero-points, is approximately 150 μm. The main lobe approximately overlaps with $\pi \times [(150/10)/2]^2 = 175$ pixels when a filter with 10-μm pixels is used, four times more with 5-μm pixels, and 16 times more with 2.5-μm pixels.

The wavefronts reconstructed by applying the Southwell procedure [30] to slope data obtained by various BPF-ODWS's for a flat input wavefront are shown in Fig. 4. The resulting peak error is 0.5 rad, 0.3 rad, and 0.15 rad for pixel size of 10 μm, 5 μm, and 2.5 μm, respectively. For two gradients along the x and y direction, the reconstruction error is symmetric along one of the bisectors. This suggests that the error results from noise generated in the detection plane by the filter that is identical for the two filter orientations. It is therefore

#260640 Received 7 Mar 2016; revised 11 Apr 2016; accepted 11 Apr 2016; published 19 Apr 2016

likely that using more than two gradients for wavefront reconstruction leads to an averaging effect of the error or detection of the resulting error for subsequent cancellation by numerical processing, but this investigation is planned for future study. For the same flat input wavefront, an ideal ODWS has insignificant root-mean-square (rms) and peak errors equal to 6×10^{-4} and 2.4×10^{-3} rad, respectively.

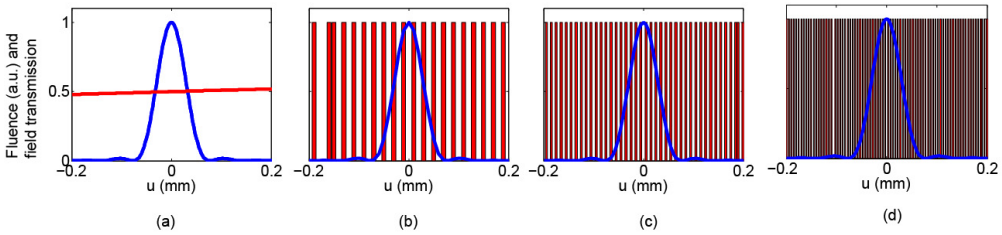

Fig. 3. (a) Transmission of a continuous linear field-transmission filter (red line), and binary pixelated filters (red bars) for pixel sizes equal to (b) 10 μm, (c) 5 μm, and (d) 2.5 μm. The lineout of the far-field fluence for a flat wavefront over the 1-cm pupil is plotted with a continuous blue line.

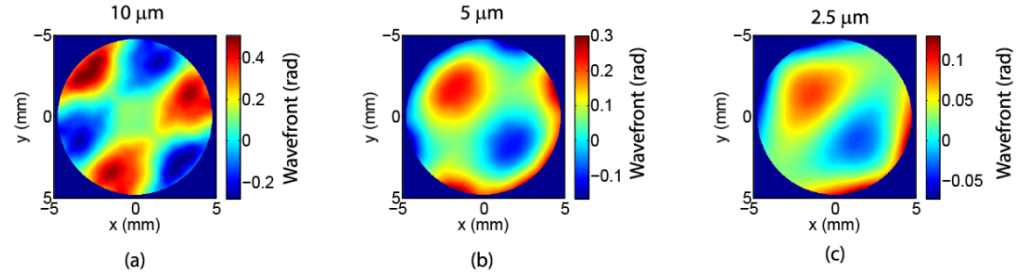

Fig. 4. Reconstructed wavefront for a flat input wavefront across a 1-cm pupil for BPF-ODWS's with filter pixel size equal to (a) 10 μm, (b) 5 μm, and (c) 2.5 μm.

Smaller pixels theoretically lead to better accuracy, but there are several practical reasons for not arbitrarily decreasing the pixel size of binary pixelated filters, and more generally beam shapers using distributions of binary pixels. Smaller pixels require tighter control of the filter fabrication to give an accurate transmission profile because a given absolute fabrication error on the pixel size yields increased relative pixel-size and transmission errors when smaller pixels are used. Pixels with size of the order of the optical wavelength or smaller lead to complex transmission phenomena that could significantly impact the filter and wavefront-sensor operation [31,32]. In this article, we limit the pixel size to 2.5 μm, i.e. approximately four times the optical wavelength $\lambda = 633$ nm.

4. Performance of a BPF-ODWS

4.1. Introduction

A BPF-ODWS is simulated and benchmarked against an ideal ODWS for various phase profiles and sensor parameters. The test wavefronts consist of sinusoidal wavefronts, wavefronts proportional to Zernike polynomials, and random wavefronts. The reconstruction performance is quantified in terms of rms and peak errors calculated over 95% of the pupil. In this section, the round pupil has a 1-cm diameter, the 4*f* line is built with lenses of focal length $f = 1$ m, and the filter width is $W = 1$ cm. This yields a dynamic range $DR \sim 100$ rad/mm, which should be of interest for a large variety of applications such as laser engineering and metrology of freeform optics.

#260640 Received 7 Mar 2016; revised 11 Apr 2016; accepted 11 Apr 2016; published 19 Apr 2016

4.2. Sinusoidal phases

The spatial phase is defined by

$$\varphi(x,y) = \varphi_0 \cos\left[2\pi\left(x\cos(\alpha) + y\sin(\alpha)\right)/p\right], \tag{7}$$

where φ_0 is the amplitude of the sinusoidal modulation, p is the spatial period, and α is the angle of the modulation relative to the x axis. The Fourier spectrum of the corresponding field is composed of isolated sidebands at wavevectors multiple of $2\pi/p$ with amplitude given by a Bessel function of the 1st kind. Although an infinite number of spectral components are generated, the most significant ones are in the interval $[-2\pi\varphi_0/p,\ 2\pi\varphi_0/p]$, and the largest wavefront slope is $2\pi\varphi_0/p$.

The results in Figs. 5 and 6 correspond to p = 1 mm, for which performance degradation due to the finite dynamic range is expected when φ_0 is of the order of 8 rad. Figures 5(a) and 5(b) show that the ideal ODWS has excellent performance, with rms and peak errors lower than λ/100 over the range of modulation amplitudes from 0 to 2π. The errors for various BPF-ODWS's over the range of φ_0 between 0 to 2π for which the errors are relatively independent of φ_0 are shown in Table 1. The error is approximately proportional to the pixel size. Figure 5(c) demonstrates that the far field spans the entire width of the filter when φ_0 = 8 rad, hence the observed ODWS performance decrease is expected.

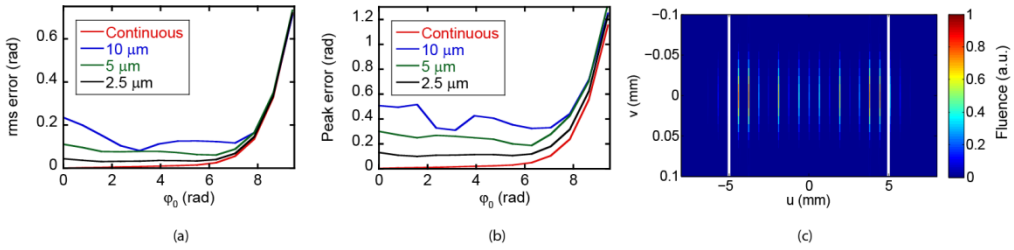

Fig. 5. (a) rms and (b) peak errors vs the amplitude of a phase modulation φ_0 for an ideal ODWS and BPF-ODWS's with pixel size equal to 10 μm, 5 μm, and 2.5 μm. (c) shows the fluence distribution in the plane of the ODWS filter for φ_0 = 8 rad, with the white lines at u = ± 5 mm indicating the edge of the filter when the gradient is in the horizontal direction.

Table 1. Averages of the peak and rms errors over the range of φ_0 from 0 to 2π

Average error (rad)	Continuous	10-μm pixels	5-μm pixels	2.5-μm pixels
Peak	0.02	0.40	0.25	0.11
rms	0.01	0.14	0.08	0.04

Results pertaining to sinusoidal modulations not oriented along one of the directions of the two linear-transmission gradients (α = 30° and α = 45°) are shown in Fig. 6 for a filter with 2.5-μm pixels and a continuous filter. Non-zero values of α lead to far-field distributions that are rotated relative to the distribution shown in Fig. 5(c). These distributions are fully encompassed in the linear region of the gradient filter oriented in the x and y directions for φ_0 = 8 rad, therefore leading to comparatively higher accuracy. Although the arbitrary choice of differentiation along x and y is adequate without some a-priori knowledge about the wavefront under test, a different choice might be more appropriate when the direction of the largest wavefront gradient is known.

#260640 Received 7 Mar 2016; revised 11 Apr 2016; accepted 11 Apr 2016; published 19 Apr 2016

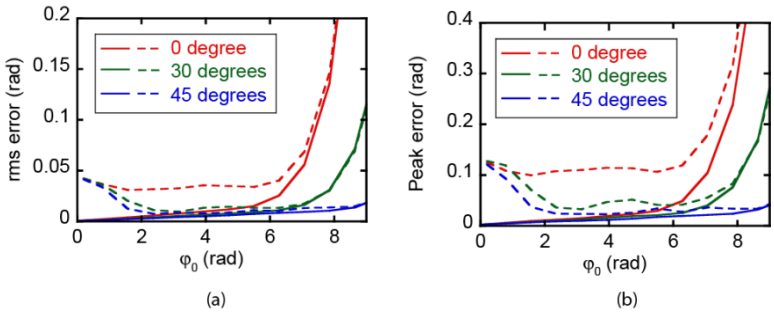

Fig. 6. (a) rms and (b) peak error for sinewaves oriented at α = 0, α = 30°, and α = 45° measured with an ODWS implemented with a continuous filter (continuous lines) and a pixelated filter with 2.5-μm pixels (dashed lines).

4.3. Zernike polynomials

A more general assessment of the ODWS performance is made using Zernike polynomials defining test wavefronts over the circular input pupil. We consider the twelve Zernike polynomials of radial order between 2 and 4 included (note that the polynomials of order 0 and 1 describe piston and tilt, respectively, which are not of interest in the context of this work), i.e., the polynomials of Noll index *j* between 4 and 15 to define the test wavefronts

$$j(r,q) = a_j Z_j(r,q). \tag{8}$$

The resulting peak and rms errors are presented in Fig. 7 for amplitude of the Zernike polynomials from 0 to 10π. For the ideal ODWS (Fig. 7, first column), the largest error is observed for spherical aberration (*j* = 11). This Zernike polynomial has the highest gradient among the considered polynomials, 1.8 rad/mm over the 1-cm pupil when a_j = 1 rad. This leads to phase gradients that span the full ODWS dynamic range for an amplitude a_j of the order of 30 radians and similar accuracy decrease for all ODWS's. The rms and peak errors for the BPF-ODWS's (Fig. 7, 2nd, 3rd, and 4th column) show that the accuracy is worst for most Zernike polynomials for amplitude between 0 and 2π radians. This is attributed to the fact that for the focal spot resulting from these wavefronts is not significantly extended on the gradient filter, which results in coverage of a relatively low number of pixels.

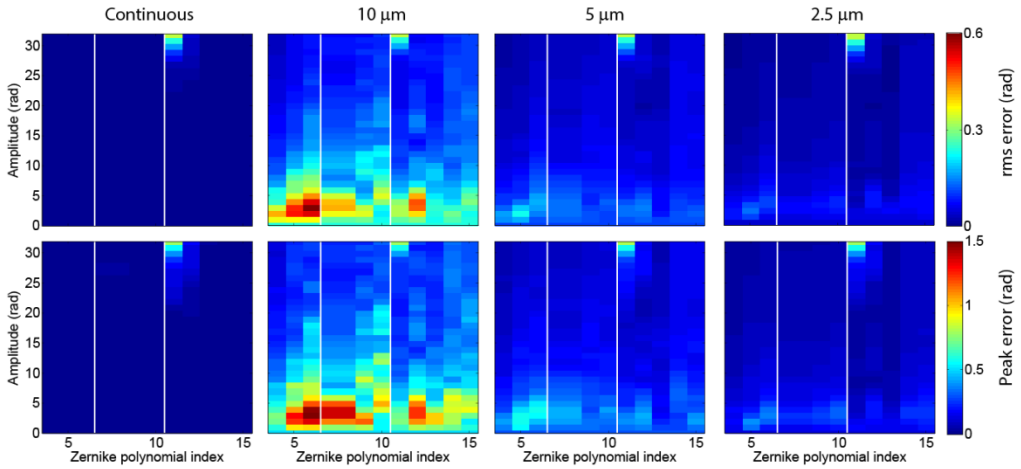

Fig. 7. rms (1st line) and peak (2nd line) errors for Zernike polynomials of Noll order j from 4 to 15 and amplitude a_j from 0 to 10π radians reconstructed by an ideal ODWS (1st column) and BPF-ODWS's based on 10-μm, 5-μm, and 2.5-μm pixels (2nd, 3rd, and 4th column, respectively). White lines have been used to separate the groups of polynomials with different orders.

#260640 Received 7 Mar 2016; revised 11 Apr 2016; accepted 11 Apr 2016; published 19 Apr 2016

Table 2 shows that the accuracy is improved significantly by decreasing the pixel size, and the statistics on the peak and rms errors are consistent with an improvement approximately equal to the change in pixel size. These statistics have been calculated over all Noll indices between 4 and 15 and amplitude between 0 and 25 radians to remain within the calculated dynamic range and avoid the inherent accuracy decrease beyond that for all ODWS's. For a filter with 2.5-μm pixels, the worst simulated peak error over the pupil is approximately 0.4 rad, i.e., λ/15.

Table 2. Statistics on the rms and peak errors, expressed in radians, for an ideal ODWS and various BPF-ODWS's measuring Zernike polynomials of Noll index between 4 and 15 and amplitude between 0 and 25 radians.

Error (rad)	Continuous	10-μm pixels	5-μm pixels	2.5-μm pixels
Average rms	1.6×10^{-3}	0.17	7.0×10^{-2}	3.6×10^{-2}
Worst rms	1.5×10^{-2}	0.59	0.23	0.14
Average peak	7.6×10^{-3}	0.50	0.21	0.11
Worst peak	0.12	1.49	0.58	0.39

4.4 Random wavefronts

Ten wavefronts were generated over the 1-cm pupil as the sum of the previous twelve Zernike polynomials with random coefficients a_j uniformly distributed between −10 and 10 radians, i.e.,

$$\varphi(r,\theta) = \sum_{j=4}^{15} a_j Z_j(r,\theta). \tag{9}$$

Each of the resulting test wavefronts (Fig. 8) was reconstructed by an ideal ODWS and various BPF-ODWS. The statistics on the reconstructed wavefronts show again that the error is approximately proportional to the pixel size (Table 3). It is interesting to note that the reconstruction error in the case of these 10 random wavefronts is in general significantly lower than in the case of the Zernike polynomials themselves.

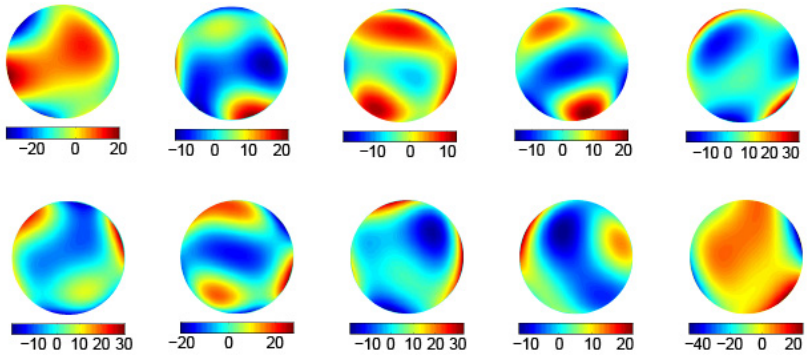

Fig. 8. Ten random wavefronts, expressed in radians, generated by linear combination of Zernike polynomials of order 2, 3, and 4 with random amplitudes uniformly between −10 and + 10 radians.

Table 3. Statistics on the rms and peak errors, expressed in radians, for an ideal ODWS and various BPF-ODWS's measuring random wavefronts obtained as linear combinations of Zernike polynomials of Noll index between 4 and 15 and random amplitude between −10 and 10 radians.

Error (rad)	Continuous	10-μm pixels	5-μm pixels	2.5-μm pixels
Average rms	3×10^{-3}	0.10	4.2×10^{-2}	1.8×10^{-2}
Worst rms	5.2×10^{-3}	0.13	6.7×10^{-2}	2.5×10^{-2}
Average peak	1.3×10^{-2}	0.33	0.12	5.8×10^{-2}
Worst peak	0.02	0.43	0.19	7.5×10^{-2}

#260640 Received 7 Mar 2016; revised 11 Apr 2016; accepted 11 Apr 2016; published 19 Apr 2016

5. Effect of pupil size and lens focal length on the BPF-ODWS performance

5.1. Effect of pupil size

For a given focal length, an increase of the pupil size leads to smaller features in the far field plane where the spatially varying transmission filter is located. This reduces the measurement accuracy when a binary pixelated filter of a given pixel size is used. Figures 9(a) and 9(b) show the rms and peak errors as a function of the amplitude of a sinewave with 1-mm period over a 2-cm pupil. The accuracy clearly decreases compared to the case of a 1-cm pupil [Figs. 5(a) and 5(b)], i.e., the error is typically a factor of two worse for the 2-cm pupil (Table 4) than for the 1-cm pupil (Table 1). As expected, the error increases when φ_0 approaches 8 radians because the dynamic range does not depend on the pupil size. When the performance decrease associated with larger pupil sizes is not acceptable, the aperture can be divided into sub-apertures that are individually characterized. The wavefront over the full aperture can then be reconstructed by stitching the corresponding sub-aperture wavefronts, as is done for interferometric measurements of optical components introducing large phase gradients [33].

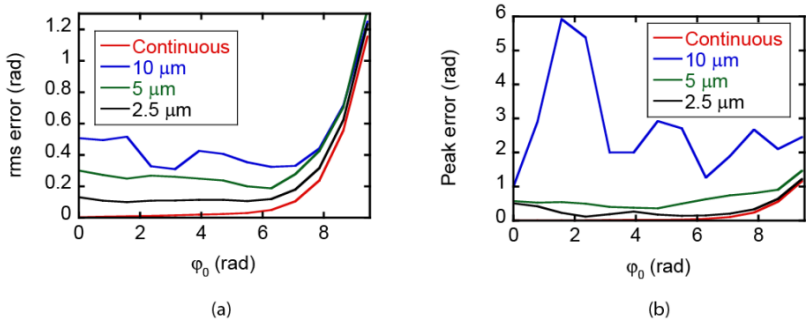

Fig. 9. (a) rms and (b) peak errors vs φ_0 for an ideal ODWS and various BPF-ODWS's for a 2-cm-diameter round pupil and f = 1 m. These plots can be compared to the plots shown in Figs. 5(a) and 5(b).

Table 4. Averages of the peak and rms errors over the range of φ_0 from 0 to 2π for a 2-cm input pupil. This table can be compared to Tables 1 and 5.

Average error (rad)	Continuous	10-μm pixels	5-μm pixels	2.5-μm pixels
Peak	9.0×10^{-3}	2.9	0.49	0.24
rms	0.10	0.8	0.18	7.8×10^{-2}

5.2. Effect of lens focal length

A change in the focal length of the ODWS modifies the scaling between wavefront slopes and spatial coordinate in the filter plane. The dynamic range is inversely proportional to the focal length, and a larger range of wavefront slopes is accommodated by the far-field filter when the focal length is decreased. A detrimental effect of the shorter focal length is that the scale of the smallest far-field feature decreases, therefore decreasing the reconstruction accuracy. Figures 10(a) and 10(b) demonstrate these effects for a 2 × reduction in focal length for the 1-mm-period sinewave wavefront profiles. No decrease in accuracy is observed beyond the amplitude value φ_0 = 8 radians, confirming the larger dynamic range, but the reconstruction error is in general larger than for the 1-m lens. Comparison of Tables 1 and 5 show that the reconstruction error is approximately inversely proportional to the focal length.

#260640 Received 7 Mar 2016; revised 11 Apr 2016; accepted 11 Apr 2016; published 19 Apr 2016

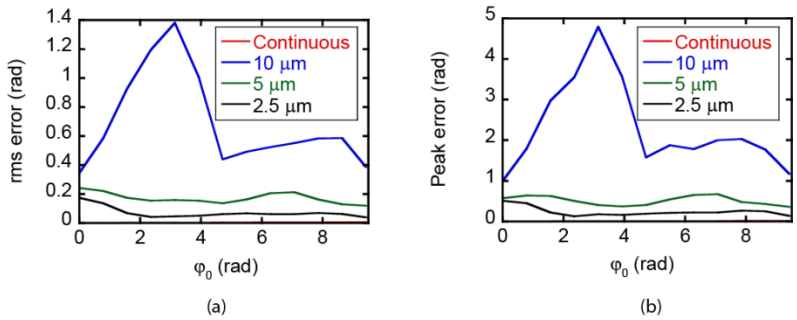

Fig. 10. (a) rms and (b) peak error vs φ_0 for an ideal ODWS and various BPF-ODWS's for a 1-cm-diameter round pupil and f = 0.5 m. These plots can be compared to the plots shown in Figs. 5(a) and 5(b).

Table 5. Averages of the peak and rms errors over the range of φ_0 from 0 to 2π for f = 0.5 m. This table can be compared to Tables 1 and 4.

Average error (rad)	Continuous	10-µm pixels	5-µm pixels	2.5-µm pixels
Peak	4.6×10^{-3}	2.54	0.52	0.25
rms	2.0×10^{-3}	0.77	0.18	7.8×10^{-2}

6. Experimental demonstration of a BPF-ODWS

6.1. Description

We have implemented a BPF-ODWS using a spatially varying transmission filter fabricated as a Cr-on-quartz lithography mask with 10-µm pixels. The measured transmission of the manufactured mask is shown in Fig. 11(a). The horizontal gradient, vertical gradient, gradient along the first and second bisector are located on the same mask to allow for measurements of the gradients F_x, F_y, F_+ and F_- by translation of the mask. These gradients were independently designed using a four-weight error-diffusion algorithm [29]. A clear zone (fluence transmission = 100%) and zone with 25% average transmission designed by error diffusion were added to the mask, allowing for a direct measurement of F_0 or $F_0/4$, respectively. Only two fluences measured with filters corresponding to orthogonal gradients and F_0 have been used for wavefront reconstruction. Alignment features have been added to facilitate translation between the different zones. The field transmission of the horizontal gradient integrated along the vertical direction is shown in Fig. 11(b).

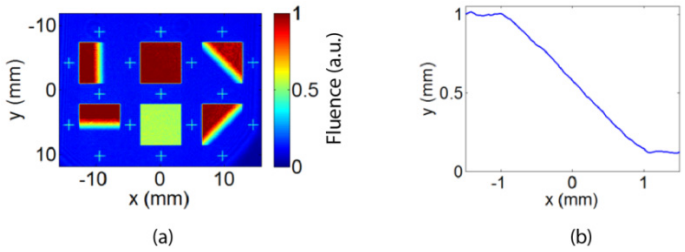

Fig. 11. (a) Spatially resolved field transmission of the mask having four gradients with different orientations, two zones with constant transmission, and alignment features. (b) Lineout of the horizontal gradient integrated along the vertical direction.

The mask has been set at the Fourier plane of a 4f line with f = 1 m. The width of each gradient is W = 2 mm. The calculated dynamic range, 20 rad/mm, is sufficient for this proof-of-concept experiment, and the relatively small value of W allows for higher sensitivity. The source under test is a HeNe laser that has been approximately collimated to a full width at half maximum equal to 1.3 mm. Because the pupil size is only a few mm, it results in a spot

#260640 Received 7 Mar 2016; revised 11 Apr 2016; accepted 11 Apr 2016; published 19 Apr 2016

size in the Fourier plane several times larger than what is obtained with the 1-cm pupil size used in the simulations. As a result, gradients with 10-µm pixels have been deemed sufficient.

6.2. Experimental results

The wavefront distortion introduced by a deformable mirror has been quantified as the difference of the wavefronts measured with and without the deformable mirror. In each situation, the wavefront of the beam has been reconstructed either with the two orthogonal gradients F_x and F_y or the two orthogonal gradients F_+ and F_-. This results in two independent determinations of the induced wavefront [Figs. 12(a) and 12(b)] that identically show the slight bending of the deformable mirror surface and actuator imprint when no voltage is applied to the actuators. The excellent agreement between these independent measurements (rms difference = 0.019λ, $\lambda = 633$ *nm*) demonstrate the consistency of the ODWS [Fig. 12(c)].

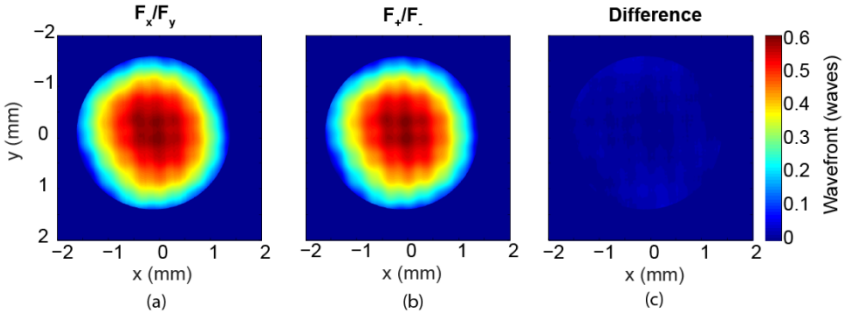

Fig. 12. Wavefront introduced by the deformable mirror reconstructed with (a) the two gradients F_x and F_y, and (b) the two gradients F_+ and F_-. (c) Difference between these two wavefronts. All wavefronts are expressed in waves.

The ODWS has been compared to a commercial Shack-Hartmann wavefront sensor (SHWS, Thorlabs WFS20-5C). The wavefront introduced by a lens (2-m focal length) has been reconstructed by differential measurements of the wavefront with and without the lens. The expected wavefront is shown in Fig. 13(a). The wavefronts measured by the ODWS and the SHWS are shown in Figs. 13(b) and 13(c). They both match the expected wavefront well, with a slightly better accuracy for the ODWS: the rms difference between the measured and calculated wavefronts is 0.047λ and 0.059λ for the ODWS and SHWS, respectively.

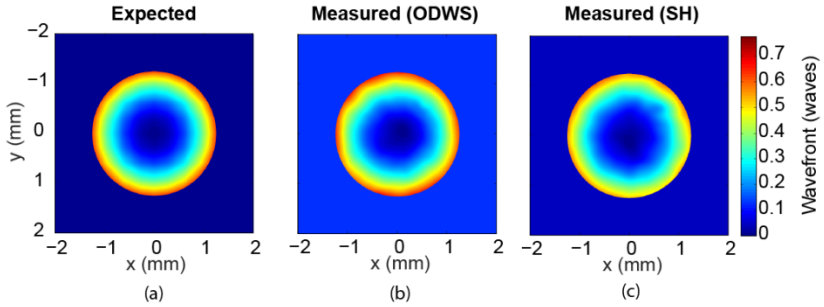

Fig. 13. Wavefront of a lens with focal length equal to 2 m (a) calculated, (b) measured with the optical differentiation wavefront sensor and (c) measured with a Shack-Hartmann wavefront sensor. All wavefronts are expressed in waves.

7. Conclusions

In conclusion, we have shown with simulations and experiments that an optical differentiation wavefront sensor reconstructing the wavefront of an optical wave from two gradients can be implemented with a binary pixelated filter synthesizing a continuous linear gradient in the far field. A baseline comparison has been established with an ODWS based on an ideal

#260640 Received 7 Mar 2016; revised 11 Apr 2016; accepted 11 Apr 2016; published 19 Apr 2016

continuous filter. It has been shown that the reconstruction error for various types of wavefronts is approximately proportional to the pixel size. The accuracy has been shown to decrease when the pupil size is increased and when the focal length of the 4*f* system in which the filter is located is reduced, with the reconstruction error being approximately proportional to the pupil size and inversely proportional to the focal length. Both effects are attributed to the smaller extent of the pupil far field that encompasses a smaller number of pixels of the pixelated filter.

Binary pixelated filters can be manufactured with high accuracy using standard commercial lithography techniques. Commercial lithography masks are accurately fabricated with multi-inch aperture, and this approach therefore allows for large-scale gradient filters that are required for high-dynamic-range measurements. Additionally, the feature size of commercial lithography masks can be controlled accurately at the micrometer level. We are currently implementing a prototype BPF-ODWS with W = 1 cm and 2.5-μm pixels to demonstrate its use for characterizing freeform optics with large phase gradients. Investigations of the use of aperture stitching in the context of the ODWS, practical considerations for simultaneous measurements of two orthogonal wavefront gradients, and use of more than two wavefront gradients are underway. Experimental and theoretical performance comparison with a Shack-Hartmann wavefront sensor in terms of dynamic range and signal-to-noise ratio are also being performed.

Acknowledgments

The authors acknowledge the contribution from A. Schweinsberg on the initial experimental setup. This work was supported by the first author's new-faculty startup fund provided by the Rochester Institute of Technology.

#260640 Received 7 Mar 2016; revised 11 Apr 2016; accepted 11 Apr 2016; published 19 Apr 2016